In situ fabrication of a titanium-niobium alloy with tailored microstructures, enhanced mechanical properties and biocompatibility by using selective laser melting

Danlei Zhao [a], Changjun Han [b], Jingjing Li [a], Jie Liu [a], Qingsong Wei [a*]*

[a] *State Key Lab of Materials Processing and Die & Mould Technology, School of Materials Science and Engineering, Huazhong University of Science and Technology, Wuhan 430074, China*

[b] *Singapore Centre for 3D Printing, School of Mechanical and Aerospace Engineering, Nanyang Technological University, 639798, Singapore*

Abstract

A titanium-niobium (Ti-Nb) alloy with tailored microstructures, enhanced mechanical properties and biocompatibility was *in situ* fabricated by selective laser melting (SLM) using a blended powder with 25 wt% Nb content. The effect of laser energy density from 70 J/mm^3 to 110 J/mm^3 on the phase transformation, microstructure, and mechanical properties of the SLM-printed Ti-25Nb alloy was investigated. The results indicate that the energy density of 110 J/mm^3 results in the highest relative density and homogeneous element distributions in the alloy. The α' and β phases with an orientation relationship of [023]β // [-12-16]α' were identified through X-ray diffraction and transmission electron microscopy, and their proportions are crucially determined by the laser energy density. With an increase in the energy density, the microstructure of the Ti-25Nb alloy varies from acicular-shaped grains to coarsened lath-shaped grains and to lath-shaped grain + celluar-shaped subgrains, due to the decrease in cooling rate and the rise in temperature gradient. The yield strength and microhardness of the printed Ti-25Nb alloy decrease with the increase in energy density from 70 J/mm^3 to 100 J/mm^3, and then increase to the highest values of 645 MPa and 264 HV at 110 J/mm^3, respectively. This variation of mechanical properties is dependent on both the coarsening of α' phase and the formation of β (Ti, Nb) solid solution. Besides, the SLM-printed Ti-25Nb alloy exhibits both the excellent *in vitro* apatite-forming capability and better cell spread and proliferation compared to pure Ti.

Keywords: Titanium-niobium alloy; selective laser melting; additive manufacturing; energy density.

* Corresponding authors: Changjun Han, cjhan@ntu.edu.sg; Tel.: +86-13667208949.
Qingsong Wei, wqs_xn@163.com Tel.: +86-13296512995.

1. Introduction

Titanium-niobium (Ti-Nb) alloys have been appealing as the alternative materials for implantology and arthroplasty applications due to their non-cytotoxicity, superb corrosion resistance, mechanical compatibility and *in vivo* osseointegration [1-3]. As one of the β phase stabilizers, Nb element has the lower melting point (2477 ℃) and less melting absorption energy than both Ta and Mo elements, endowing Ti-Nb alloys a better workability [4, 5]. On the other hand, the excellent ductility of Ti-Nb alloys prevents the initiation of cracks during compression and contributes to the longevity of implants [6]. In addition, the Nb_2O_5 formed on Ti-Nb surfaces facilitates the growth and proliferation of osteoblasts by improving the hydrophilia and increasing the quantity of hydroxide radical [7].

Conventional manufacturing processes, such as cast and free forging, have been utilized for the fabrication of Ti-Nb alloys [8, 9]. However, it is difficult to obtain homogeneous microstructure in the alloys without any element segregations, which is derived from remarkable differences of melting points and densities between Ti and Nb [8-10]. Therefore, additive manufacturing (AM), based on a successively layer-by-layer fashion, has been increasingly explored to manufacture Ti-Nb parts from computer-aided design (CAD) models. Both a high energy input into a tiny melt pool with high temperatures (above 3000 ℃) and a strong convection induced by a large temperature gradient in the melt pool can promote the diffusion between Ti and Nb, contributing to the homogeneity of elements and microstructure [11]. Selective laser melting (SLM), electron beam melting (EBM) and directed energy deposition (DED) are the major AM processes to fabricate Ti-Nb parts using pre-alloyed powders or mechanically blended powders of Ti and Nb. For example, Fischer *et al.* utilized DED to fabricate a Ti-27.5Nb (at%) alloy with an improved cytocompatibility and mechanical biocompatibility using a wire-arc atomized pre-alloyed powder, and found that the grain morphologies were determined by thermal history and part geometry [12]. Liu *et al.* investigated the compressive and fatigue behaviors of Ti-24Nb-4Zr-8Sn porous structures fabricated by EBM using a gas-atomized powder, indicating that the microstructure of the alloy led to greater plastic zone ahead of the fatigue crack tip compared to that of Ti6Al4V [13].

SLM has been the most popular AM process to *in situ* fabricate Ti-Nb alloys using blended powders of Ti and Nb. It can not only realize the *in situ* alloying of Ti and Nb to achieve a strong metallurgical bonding with homogenous element distributions, but also suit for the manufacture of customized bone implants or prostheses with refined and complex structures [14-16]. Researches have been focused on SLM-printed Ti-Nb alloys with a wide range of Nb content (15–45 at%) with regard to microstructure and mechanical properties [17-19]. Fischer *et al.* utilized SLM to manufacture a Ti-26Nb (at%) alloy with different process parameters and illustrated that the laser energy crucially influenced the compactness and homogeneity of the alloy [19]. Wei *et al.* also developed a Ti-26Nb (at%) alloy using SLM and achieved a balance between the strength of 646 MPa and the ductility of 21.6% for the alloy through heat treatments [18]. Wang *et al.* investigated the effect of Nb content ranging from 15 at% to 45 at% on the microstructure, mechanical strength and biomedical properties of SLM-printed Ti-Nb alloys, and obtained the highest strength of 1030 MPa and superb apatite-forming capability in the Ti-45Nb alloy [1]. Moreover, Wang *et al.* explored the availability of the mixture of elemental powders and the chemical homogeneity of a Ti-35Nb alloy fabricated by SLM [17]. They elucidated that the chemical heterogeneity of undissolved Nb particles resulted in the mechanical and chemical instability of the alloy.

During the SLM process, powder materials undergo repeated heating and non-equilibrium solidification with complicated thermal histories. The final quality and mechanical properties of printed parts are dependent on powder properties and process parameters [20]. The laser energy input controls the degree of consolidation of powder particles and the formation of defects by creating turbulences in melt pools. An excessive energy input resulted in circular or spherical pores, while insufficient energy input led to micro-voids or narrow cracks oriented perpendicularly to the build direction [21]. The optimization of process parameters is beneficial to minimizing these defects in the parts, thus enhancing their mechanical properties [22, 23]. Few studies are focused on the effect of energy density on the microstructure and mechanical properties of Ti-Nb parts *in situ* fabricated by SLM using a blended powder. Especially, the laser energy input determines the heat transfer and fluid flow in melt pools as well as the

diffusion between Ti and Nb elements, resulting in the melt pool instability and resultant distinctive microstructures and mechanical properties of Ti-Nb alloys.

In this work, the effect of laser volumetric energy density on the printability, phase transformation, microstructure and mechanical properties of a Ti-Nb alloy *in situ* fabricated by SLM was investigated. Since Ti-based alloys with α + β phases were demonstrated to possess favorable comprehensive properties with high strength and good ductility [24]. Therefore, Ti-25Nb (wt%) was designed for achieving α + β dual phases with homogeneous element distributions. The underlying mechanisms of microstructure and property variations of the printed Ti-Nb alloy at different energy densities were revealed. The *in vitro* biocompatibility of the printed alloy was preliminarily evaluated through the immersion testing in the simulated body fluid and cell culture.

2. Materials and methods

2.1. Material preparation

A gas-atomized commercially pure Ti powder (CP Ti, AP&C, Canada) and a mechanically crushed Nb powder (Puwei, China) were used. The spherical Ti powder particles and irregular Nb powder particles were characterized by scanning electron microscope (SEM, JSM-7600F, JEOL, Japan), as shown in Figs. 1a and b. The Ti and Nb powders were blended with the 25 wt% Nb content in a QM-3SP4 planetary ball mill equipment under a high purity argon atmosphere using the ball-to-powder weight ratio of 5:1 at the rotation speed of 300 rpm for 2 h. The Nb powder particles were distributed around the spherical Ti powder particles (Fig. 1c). The particle size distribution of the blended powder was analyzed using a particle size analyzer (Worcestershire, UK), and the average particle size *Dv*50 was measured as 31.4 μm.

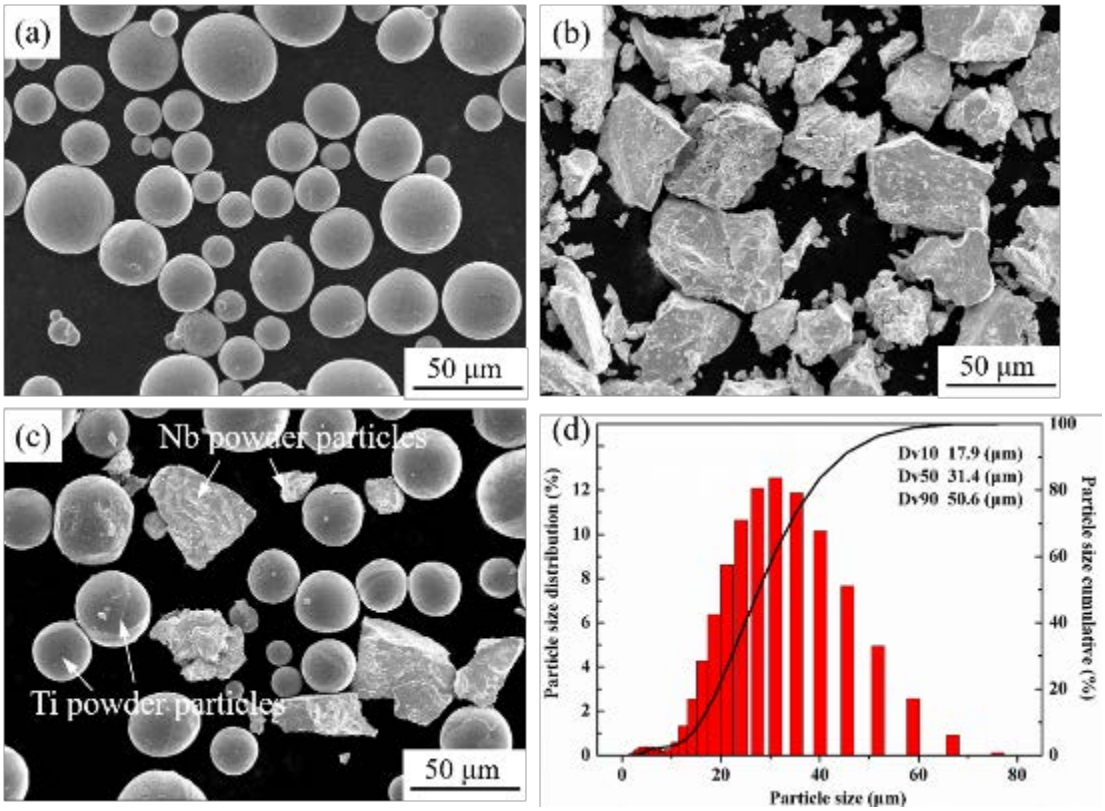

Fig. 1. SEM images showing powder morphologies: (a) Ti, (b) Nb, and (c) Ti-25Nb; (d) particle size distribution of the blended powder.

2.2. Sample manufacturing by SLM

The Huake-250 SLM machine with a fiber laser (IPG, USA) having a maximum power of 500 W and a spot size of ~100 μm was used for the *in situ* fabrication of Ti-25Nb alloy with the blended powder. The schematic illustration of SLM is shown in Fig. 2a. During the SLM process, the chamber was filled with a high-purity argon to prevent the oxidation of samples. A bi-directional scanning strategy was used in each layer, and a 90° rotation was applied between adjacent two layers.

The volumetric energy density *E*, defined as the averaged applied energy per volume of material during the scanning of one layer, is used to investigate the synthetic effect of process parameters by

$$E = \frac{P}{vht}, \tag{1}$$

where *P* is the laser power (W), *v* the laser scanning velocity (mm/s), *h* the hatch spacing (mm) and *t* the layer thickness (mm). The *P* was in the range of 210–330 W with the

fixed *v* of 1000 mm/s, *h* of 100 μm and *t* of 30 μm. Five different energy densities were denoted as E1 (70 J/mm^3), E2 (80 J/mm^3), E3 (90 J/mm^3), E4 (100 J/mm^3) and E5 (110 J/mm^3). These parameters were utilized to print cubic samples with the dimension of 10 mm × 10 mm × 10 mm and tensile coupons with the length of 32 mm, width of 7 mm and the gauge length of 10 mm (Fig. 2b).

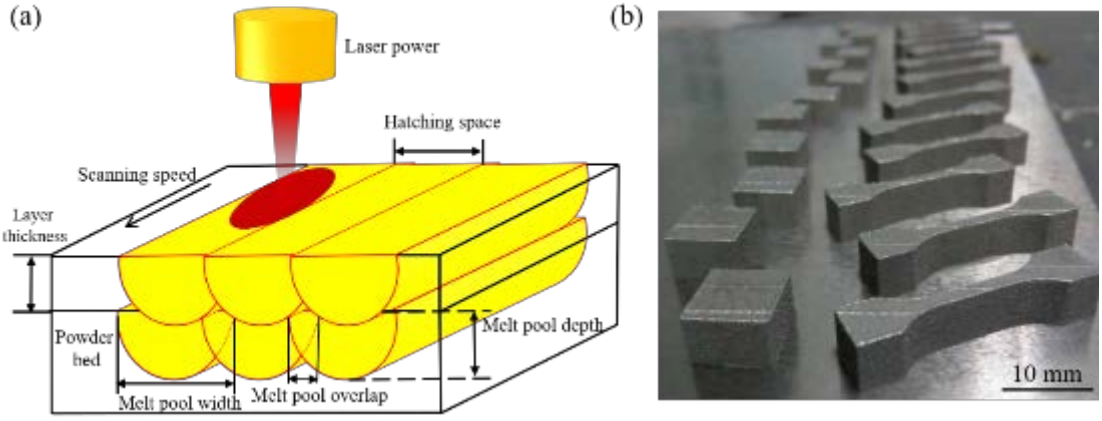

Fig. 2. (a) Schematic illustration of SLM and (b) printed Ti-25Nb parts using different energy densities.

2.3. Characterizations

The relative densities of the printed Ti-25Nb samples were determined by the Archimedes' principle. The experimental density ρ_s of the samples was calculated by $\rho_s = M_{air}/(M_{air} - M_{water})$, and the relative density was defined by the value of ρ_s/ρ_{theory}, where M_{air} is the mass of samples in air, M_{water} the mass of samples in water, and ρ_{theory} the theoretical density of Ti-25Nb. The ρ_{theory} of 5.10 g/cm^3 was measured from the true density of the blended powder. The average values were calculated from three samples for each energy density. The printed cubic samples were ground, polished and etched with the Kroll's reagent (2 mL HF, 6 mL HNO_3 and 92 mL distilled water) for microstructure characterization. The microstructure of the samples was examined by scanning electron microscope (SEM, JSM-7600F, JEOL, Japan) equipped with an energy dispersive spectroscopy (EDS) system. The phases were identified using X-ray diffraction (XRD, XRD-7000S, Shimadzu, Japan). The diffraction angle of 2θ varied from 30° to 90° with a continuous scanning rate at 10° min^{-1}. Transmission electron microscope (TEM) and high-resolution transmission electron microscope (HRTEM)

characterizations were performed on a JEOL-2100 type equipment (JEOL, Japan).

2.4. Mechanical testing

A 430-SVD hardness test machine with a load of 1.0 N and dwell time of 15 s was used to measure the Vickers hardness. Five points at different positions of the printed samples were tested to obtain an average value for each energy density. Additionally, the tensile testing was performed on a Zwick/Roell z020 (Germany) machine with three samples for each energy density.

2.5. Biocompatibility testing

The *in vitro* bioactivity of the printed Ti-25Nb alloy was evaluated by executing the apatite-forming capability after being soaked in the simulated body fluid (SBF) solution at the body temperature for 2 weeks. The formulation of SBF solution was listed in Table 1 and the pH value of SBF solution was adjusted to 7.4 [25]. Before the immersion in the SBF, samples were polished and cleaned in the distilled water, alcohol and acetone. Surface morphologies of the samples before and after the immersion were examined by SEM and EDS.

Table 1. The formulation of SBF solution.

Order of addition	Reagent	Molar mass (g/mol)	Content (g)
1	NaCl	58.440	8.035
2	$NaHCO_3$	84.008	0.355
3	KCl	74.460	0.225
4	$K_2HPO_4 \cdot 3H_2O$	228.046	0.231
5	$MgCl_2 \cdot 6H_2O$	203.306	0.311
6	$CaCl_2$	110.980	0.292
7	Na_2SO_4	142.040	0.072

The initial cell response of the alloy was investigated through cell culture. MC3T3-E1 (ATCC, USA) were seeded in the Alpha Modification (α-MEM, HyClone, USA) with the 10% FBS (fetal bovine serum) at 37 °C in a humidified 5% CO_2 atmosphere.

The cubic samples were ultrasonically cleaned with acetone and absolute ethanol and then steam sterilized. These samples were seeded at a cell density of 235000 cells/cm^2. After 48 h of cell culture, seeded samples were rinsed with PBS (phosphate buffer saline) twice and 20 min per time, and fixed with 2.5% glutaraldehyde at 4 °C for 4 h and two times. The pure Ti samples were seeded as the blank group for comparison. The cells growing on the two samples that were dried with calcium chloride and sputter-coated with Au were observed using SEM. For the immunofluorescence, both of the samples were stained with phalloidin for 20 min, and then the nuclei were stained with DAPI for 5 min. The images were captured by a confocal microscope.

3. Results and discussion

3.1. Density and chemical homogeneity

The relative densities of SLM-printed Ti-25Nb samples with different laser energy densities are greater than 96.5% (Fig. 3a). The huge differences of melting and boiling points between Ti and Nb hinder the achievement of a near-full density for the printed Ti-25Nb alloy. As a result, a greater energy density of SLM is required for the printing of Ti-Nb alloys compared to pure Ti. This leads to the preferential vaporization of Ti within melt pools and resultant keyhole pore formation. Meanwhile, small Ti particles with a dimension of a few microns appeared due to the striking during ball milling (Fig. 1c). These small particles are liable to sputter under the impact of laser during SLM and located on the surface of a solidified printed layer, thereby producing a rough surface that is detrimental to the fusion between adjacent layers and forming pores. Compared to the pure Ti powder with a high degree of sphericity, the blended powder with an irregular morphology has a lower loose packing density and worse flowability, which is potential to form pores due to the insufficient liquid in large voids between powder particles [26].

Applying the energy density of E5 (110 J/mm^3) leads to the highest relative density of 97.5 % for the printed Ti-25Nb alloy. During SLM, the dynamic viscosity μ of molten metals can be determined by

$$\mu = \frac{16}{15}\sqrt{\frac{m}{k_B T}}\gamma\,, \tag{2}$$

where m is the atomic mass, k_B the Boltzmann′s constant and γ the liquid surface tension [27]. According to Eq. (2), the increase of energy density reduces the dynamic viscosity of liquid, which accelerates its flow to fill in pores and improves the densification. As presented in Figs. 3b and c, the Ti-25Nb alloy printed using the lowest relative density of 70 J/mm^3 exhibits micro-cracks and pores. The cracks with the length of ~10 μm resulted from thermal residual stresses induced by large temperature gradients [28]. The pores appear ellipsoidal with the size of 2–5 μm due to the gas precipitation in melt pools and gas transfer from the powder [29].

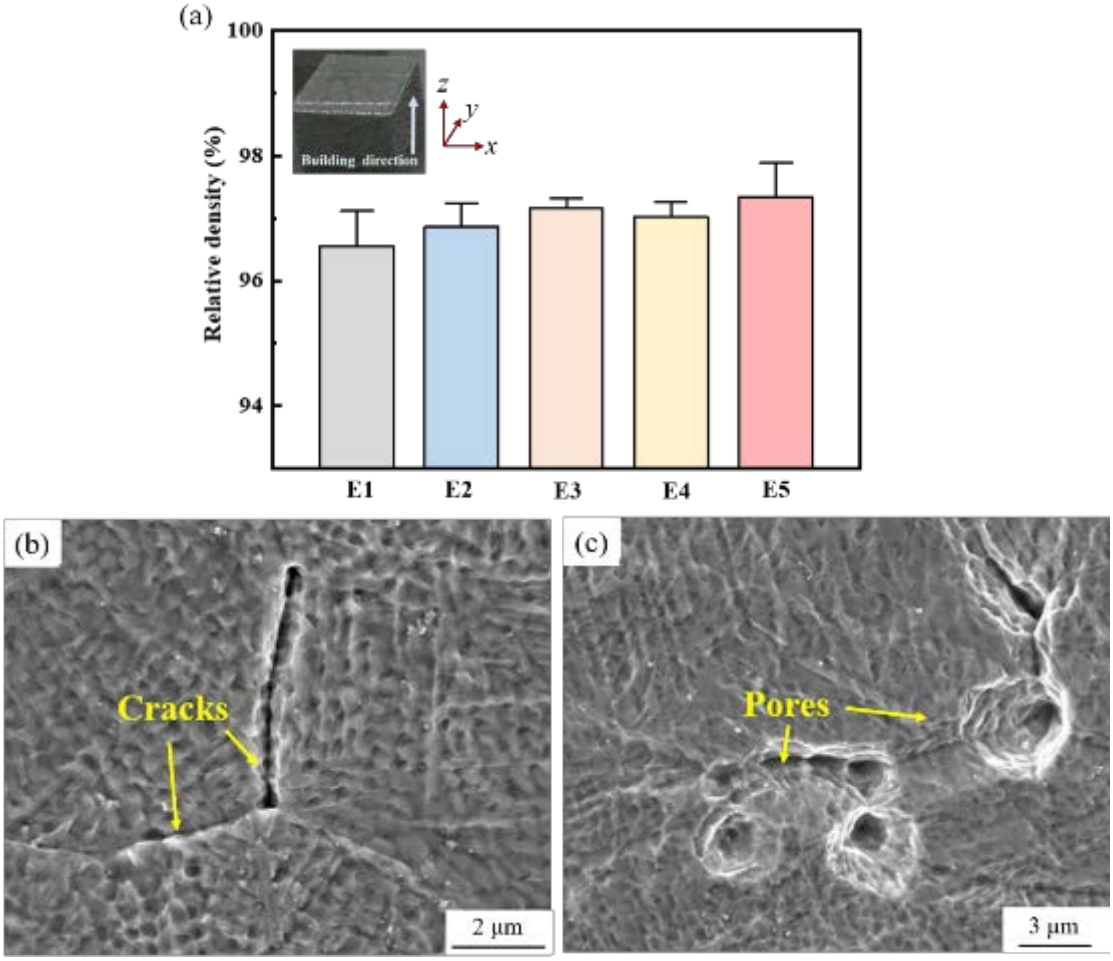

Fig. 3. (a) Relative densities of the Ti-25Nb samples *in situ* fabricated by SLM with different energy densities, (b) and (c) cracks and pores in the sample at the energy density of E1 (70 J/mm^3), respectively.

Fig. 4 exhibits the surface morphologies of Ti-25Nb samples at energy densities of E1 and E5. Since the center of applied Gaussian beam has greater energy than the edge, the edge of the laser beam provides insufficient energy for Nb particles to be fully melted and diffuse into the Ti matrix. As illustrated by Polozov *et al.*, the energy density played a critical role in the amount of unmelted Nb particles and the microstructure of alloys [30]. The partially melted Nb can be found in the alloy at the energy density of E1 through the EDS analysis (Fig. 4a), indicating the insufficient dissolution and diffusion of Nb. Comparatively, the printed Ti-25Nb alloy presents homogeneous element distributions at the energy density of E5 (Fig. 4b). ~~[31].~~ In SLM, large temperature gradients contribute to the rise in surface tension and resultant Marangoni convection [28]. The high energy density of E5 accelerates the convection in melt pools and improves the diffusion between Ti and Nb elements. On the contrary, the low energy density alleviates the melt flow with a high viscosity [32], which limits the element diffusion and retains the unmelted Nb particles in the alloy. It can be concluded that a high energy density can be beneficial to improving the element homogeneity and relative density of the Ti-25Nb alloy printed by SLM.

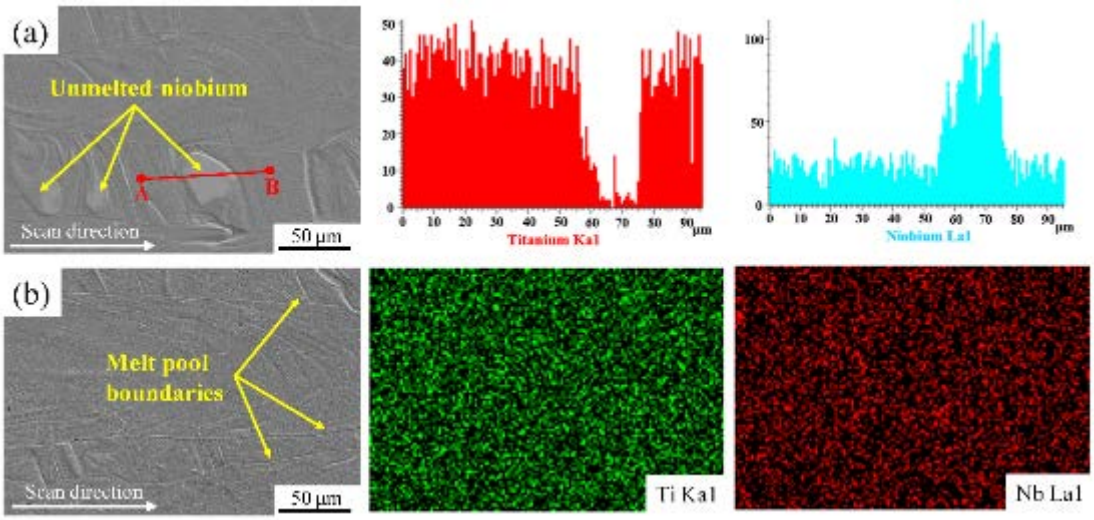

Fig. 4. Surface morphologies and element distributions of SLM-pritned Ti-25Nb samples using different energy densities in the *x-y* plane from SEM and EDS analysis: (a) E1 (70 J/mm^3) and (b) E5 (110 J/mm^3).

3.2. Phase identification

Fig. 5 exhibits the XRD patterns and phase proportions of SLM-printed Ti-25Nb

samples with different energy densities. As a β phase stabilizer, the Nb element is able to reduce both the phase transformation temperature from β to α and the critical cooling rate for retaining β [33]. Fig. 5a indicates the formation of hexagonal close-packed (hcp) α' martensite phase and body-centered cubic (bcc) β phase in the printed alloy. The energy density plays a crucial role in the proportions of phases, which can be calculated by the Reference Intensity Ratio (RIR) method [34]. The method allows to evaluate the variation regularity of each phase in the printed alloy with different energy densities. As displayed in Fig. 5b, the proportion of α' phase increases from 43% to 52% with the rise in energy density from 70 J/mm^3 to 90 J/mm^3, and decreases to 41% when the energy density increases to 110 J/mm^3. Phase transformations occurred in the SLM-printed Ti-25Nb samples are dependent on the energy density.

According to the Ti-Nb binary phase diagram, phase transforms from β to α in the Ti-25Nb alloy during solidification [35]. However, the high cooling rate of 10^3–10^6 K s^{-1} in SLM contributes to the formation of metastable phases [36, 37]. The martensitic transformation depends on the driving force $\Delta G_{\mathrm{v}}^{\beta\to\alpha'}$ calculated by

$$\Delta G_{\mathrm{v}}^{\beta\to\alpha'}\left(T_{\mathrm{c}}\right)=\frac{\Delta H_{\mathrm{v}}^{\beta\to\alpha'}\left(T_0\right)\left(\Delta T\right)}{T_0}, \tag{3}$$

where T_0 is the phase equilibrium temperature (℃), T_{c} the transient temperature (℃), $\Delta H_{\mathrm{v}}^{\beta\to\alpha'}\left(T_0\right)$ the heat of fusion (J mol^{-1}), and $\Delta T=T_{\mathrm{c}}-T_0$ the degree of superheat [33]. When $T_{\mathrm{c}} > T_0$, the transformation of $\beta\to\alpha'$ occurs. According to Eq. (3), the driving forces for phase transformation are proportional to the degree of superheat. A high energy density leads to the high transient temperature of melting pools, increasing the degree of superheat and driving forces of phase transformation. Thus, the increment in energy density from E1 to E4 facilitates the martensitic transformation and retains more α' phases in the Ti-25Nb samples. However, with the energy density of E5, the formation of β(Ti, Nb) solid solutions is promoted due to the sufficient melting of Nb particles, which reduces the proportion of α' phase.

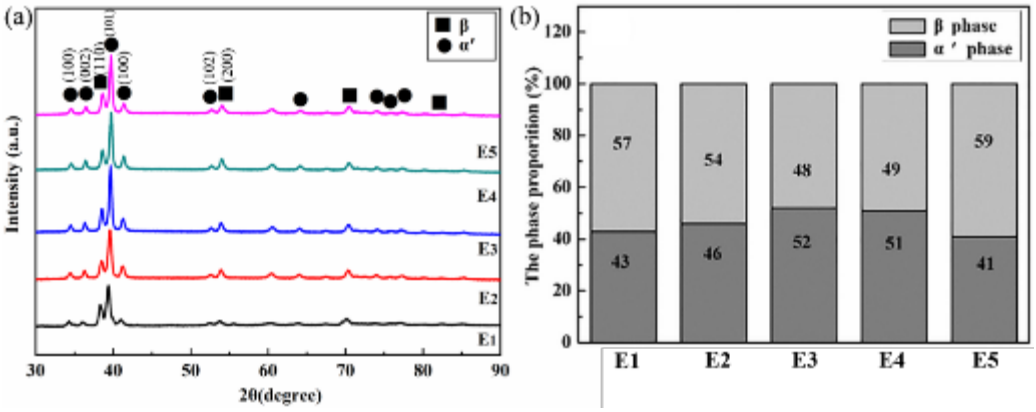

Fig. 5. (a) XRD patterns of the Ti-25Nb alloys printed by SLM with different energy densities and (b) the proportions of each phase.

3.3. Microstructure

Fig. 6 shows the microstructures of the SLM-printed Ti-25Nb samples with the increase in energy density. The acicular-shaped grains can be observed at low energy densities (70-80 J/mm^3), corresponding to α' phase (Figs. 6a and b). As the energy density increases to 90 and 100 J/mm^3, the martensite grains grow up to the coarsened lath shape (Figs. 6c and d). Simlar coarse grains in Ti-13Nb-13Zr alloys can also be found at the energy density of 92.59 J/mm^3 [3]. Furthermore, the cellular-shaped subgrains appear at the energy density of 110 J/mm^3 (Fig. 6e). Therefore, with the rise in energy density, the microstructure of the printed Ti-25Nb samples changes from acicular-shaped grains to coarsened lath-shaped grains and to lath-shaped grains + cellular-shaped subgrains.

The grain size is denpendent on the cooling rate R calculated by

$$R = -2\pi\lambda c\rho \frac{\left(T_c - T_0\right)^3}{\left(E_L / \delta\right)^2}, \tag{4}$$

where E_L is the line energy density (J/mm), δ the thickness of plate (mm), λ the thermal conductivity [W/(mm·℃)], c the specific volume heat [J/(g·℃)], ρ the density of material (g/mm^3), T_c the transient temperature (℃), and T_0 the initial temperature (℃) [38]. Thus, the increase of energy density reduces R, coarsening the microstructure of the Ti-25Nb alloy. The further increase in energy density enhances both the temperature gradient G in melt pools and the element diffusion. As a result, a cellular solidification

occurs under a large *G*/*R* from E5 (Fig. 6f), leading to the formation of cellular subgrains. Meanwhile, the sufficient melting of Nb facilitates the diffusion of Nb into Ti matrix and the constitutional undercooling in the solute redistribution. The constitutional undercooling also induces a solid-liquid interface instability, acting as an additional driving force to facilitate the nucleation of finer cellular β grains.

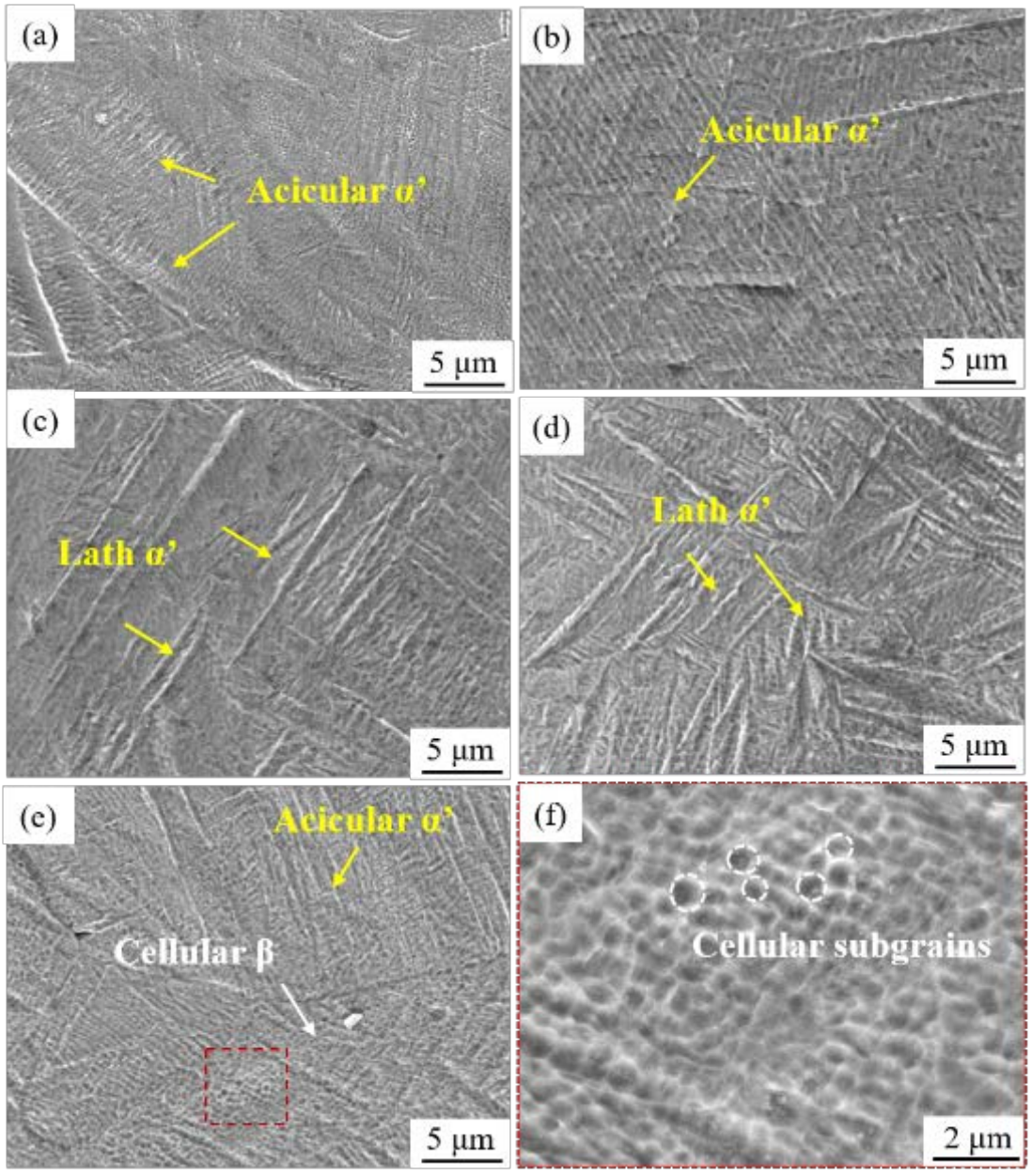

Fig. 6. Microstructures of the SLM-printed Ti-25Nb samples at different energy densities in the *x*-*y* plane observed by SEM: (a) E1 (70 J/mm^3), (b) E2 (80 J/mm^3), (c) E3 (90 J/mm^3), (d) E4 (100 J/mm^3), (e) and (f) E5 (110 J/mm^3).

Fig. 7 depicts typical morphologies of the samples at the energy density of E5 in

different planes. The melt pool boundaries (MPBs) can be observed in both of the two planes. The acicular martensitic grains appear in each of the β grain, indicating that martensitic transformation occurs from prior β grain boundaries. The elongated β grains present epitaxial growth across MPBs along the building direction in the *x*-*z* plane (Fig. 7a). The average length of β grains is ~100 μm, and acicular α' grains with a length of 20–50 μm exist in the β grains. The variation of grain morphology is attributed to different thermal histories in two planes. During SLM, the grains grow epitaxially due to the absence of nucleation barriers to solidification and the partial re-melting of previously consolidated layers [39]. In the *x*-*y* plane, smaller β grains can be found in melt pools compared to those in the *x*-*z* plane (Fig. 7b), which indicates the microstructure anisotropy of the SLM-printed Ti-25Nb alloy.

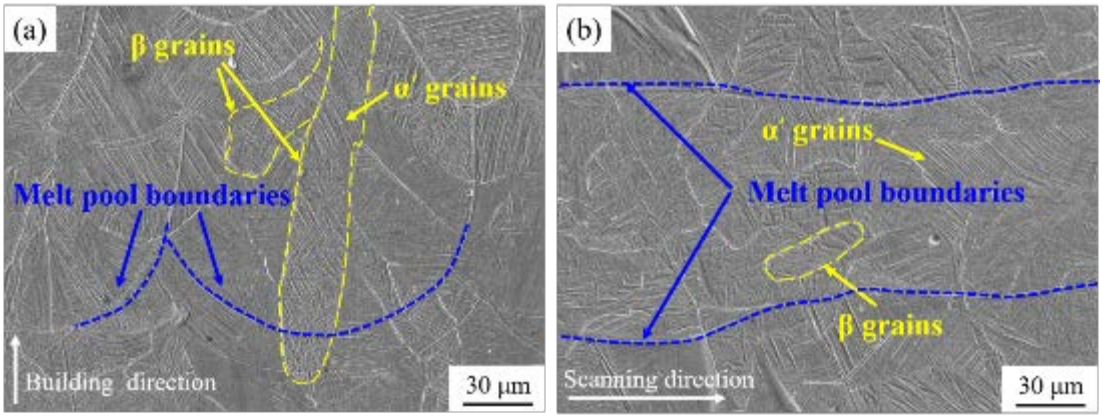

Fig. 7. Microstructure of the SLM-printed Ti-25Nb alloy in different planes at the energy density of E5 (110 J/mm^3): (a) *x*-*z* plane and (b) *x*-*y* plane.

The formed β and α' phases in the Ti-25Nb alloy are further validated through TEM. Fig. 8a exhibits that the acicular-like α' martensites are precipitated in the β phase with a width of ~100 nm. Fig. 8b shows the electron diffaction pattern with the zone axis of [023]β, indicating that the α' phase (marked as red) coexists with the retained β phase (marked as yellow). One of the orientation relationships between β phase and α' phase is [023]β // [-12-16]α'. The phase boundary between α' and β can be recognized (Fig. 8c). The inter-planar spacings are 0.158 nm for (200)β and 0.255 nm for (10-10)α' from HRTEM. In Fig. 8d, dark areas in the HAADF image consist of α' and light areas contain β. In particular, nano-twinning can be discovered in the printed Ti-25Nb alloy

(Figs. 8e and f), which resulted from the phase transformation and complex residual stresses in SLM [40, 41]. Regarding the phase transformation, orthorhombic martensite α″ phase could be found in quenched Ti-Nb alloys [42]. Lee *et al*. exhibited that the splitting of XRD peaks was a direct indication for the existence of α″ phase [43]. However, the α″ phase could not be observed in the SLM-printed Ti-25Nb alloy according to XRD and TEM results. On the other hand, the α′ phase could be recognized with long martensitic plates with an acicular morphology [44], twins and a substructure with dislocations [45], which is dominant in the SLM-printed Ti-25Nb alloy.

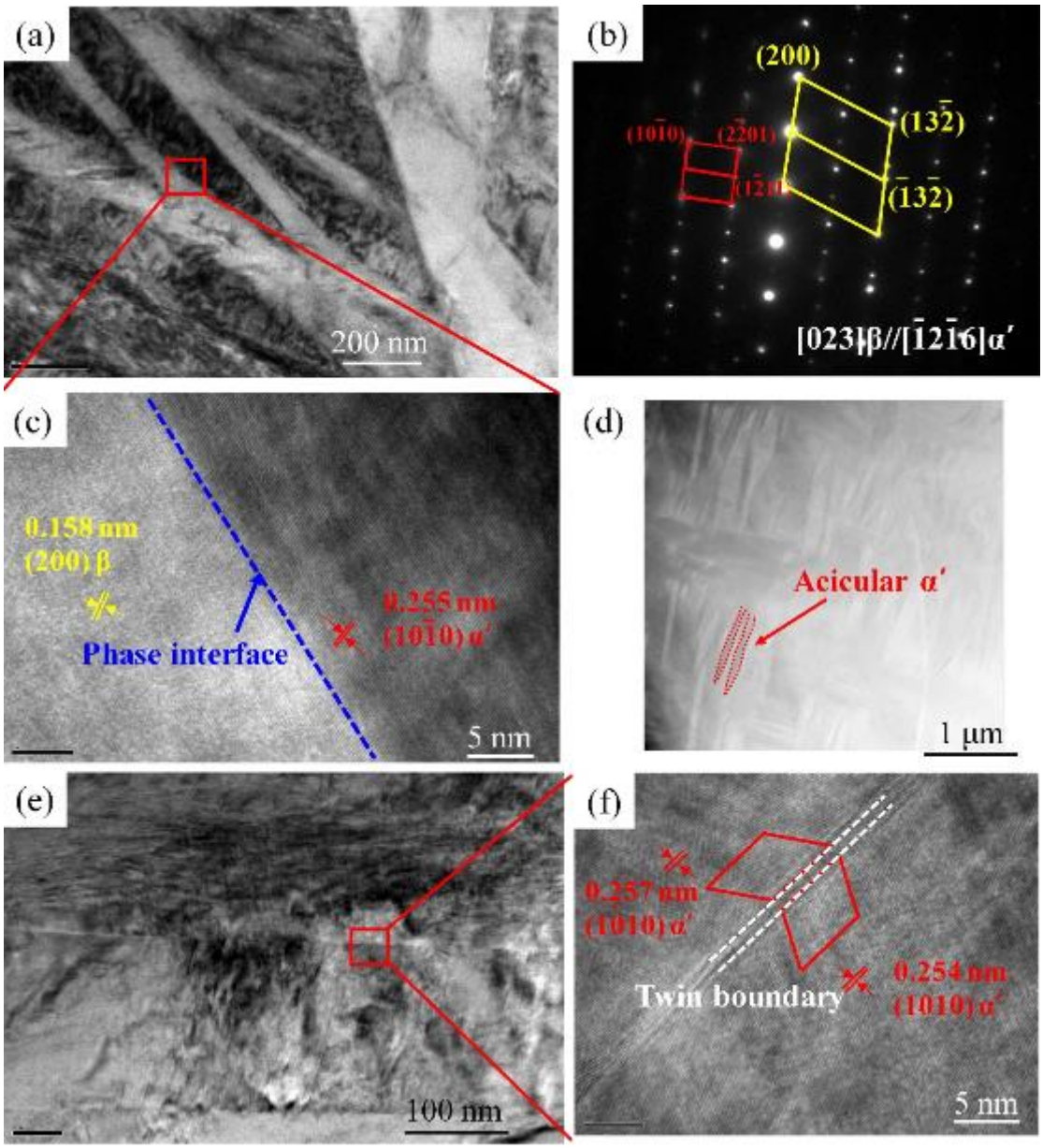

Fig. 8. TEM analysis on the phase components of the SLM-printed Ti-25Nb alloy at the energy density of E5: (a) Bright-field image, (b) SAD pattern, (c) HRTEM image

of the region indicated in (a), (d) HAADF image, (e) bright-field image showing nano-twins, and (f) HRTEM image of the nano-twins.

3.4. Mechanical properties

The effect of energy density on the mechanical properties of the SLM-printed Ti-25Nb alloy is illustrated in Table 2. With the increase of energy density from E1 to E4, the ultimate tensile strength, yield strength, ductility and microhardness of the alloy decrease from 740 MPa to 685 MPa, 640 MPa to 574 MPa, 19.5% to 17.3% and 261 HV to 245 HV, respectively. The Ti-25Nb alloy printed using the energy density of E5 achieves a superb combination of the high yield strength of 645 MPa, ultimate tensile strength of 748 MPa and ductility of 19.9%.

Table 2. Mechanical properties of SLM-printed Ti-25Nb alloys with different energy densities, in comparison with similar SLM-printed Ti-Nb alloys.

Samples	Yield strength (MPa)	Tensile strength (MPa)	Young's modulus (GPa)	Ductility (%)	Hardness (HV)
E1	640 ± 15	740 ± 27	84.6 ± 1.3	19.5 ± 5.5	261 ± 5
E2	612 ± 11	731 ± 14	85.7 ± 1.5	20.7 ± 1.4	250 ± 4
E3	593 ± 18	714 ± 21	88.0 ± 2.3	18.9 ± 2.0	246 ± 4
E4	574 ± 14	685 ± 6	88.7 ± 0.9	17.3 ± 2.8	245 ± 2
E5	645 ± 23	748 ± 27	83.5 ± 0.8	19.9 ± 2.1	264 ± 6
Ti-26Nb (at%) [19]	-	-	76 ± 0.4	-	268
Ti-26Nb (at%) [18]	768	799	-	14.3	-

The yield strength and hardness of the printed Ti-25Nb alloy exhibit the similar variation as the energy density increases from E1 to E5, which are determined by both the coarsening of α' phase and the formation of β (Ti, Nb) solid solution. The increase in energy density contributes to the coarsening of α' grains, and accelerates the liquid convection and the diffusion between Nb and Ti. It promotes the reduction in α' phase and the formation of β with fine cellular subgrains. According to the Hall-Petch relationship, the reduction of grain size results in the enhancement of strength [46]. From E1 to E4, the microstructure of Ti-25Nb is governed by the coarsening of α' grains,

leading to the increase in the grain size and the resultant decrease in the yield strength. However, the formation of β phase with fine cellular subgrains is dominant in the microstructure at the energy density of E5, which contributes to the enhancement of yield strength. Since the β phase has a lower modulus than α' phase, the alloy with E5 obtains the lowest Young's modulus, which is determined by the most proportion of β. In addition, the ductility of the alloy with E4 is lower than that with E1 due to the growth of α' martensitic phase. The α' phase was proved to enhance the strain hardening and decrease the ductility of alloys [36]. The ductility of the alloy with E5 is greater than that with E4, due to the increment in the β phase. The bcc structure endows β phase a better plastic deformation ability than α' phase with a hcp structure [47].

The SLM-printed Ti-25Nb alloy exhibits 14% higher microhardness and 25% higher tensile strength than casted and free-forged counterparts, respectively [8, 48]. The finer microstructure caused by the ultra-fast cooling rate in SLM is responsible for the superior mechanical properties. Furthermore, the α′ martensite phase formed in SLM is comprised of more dense interplanar crystal spacing and a higher dislocation density compared to the α phase formed in casting [49]. The high dislocation density and the twining observed by TEM also lead to strong barriers to hinder dislocation motion and improve the mechanical properties of the printed Ti-25Nb alloy. Compared to the SLM-printed Ti-26Nb alloy (at%) with 40 wt% Nb [18, 19], the printed alloy with 25 wt% Nb obtains lower strength and hardness but higher ductility due to the lower Nb content. A high Nb content contributes to the improvement of both strength and hardness, but raising the possibility of retaining unmelted Nb particles. The interface between the undissolved Nb and the Ti matrix may be detrimental to the ductility of alloys [17].

3.5. *In vitro* biocompatibility

The SBF immersion and cell culture experiments were conducted to evaluate the *in vitro* biocompatibility of the SLM-printed Ti-25Nb alloy. Figs. 9a and b present the surface morphologies of the printed samples before and after the immersion in SBF for 2 weeks. The alloy surface after SBF immersion was covered by small precipitations with the spherical shape (Fig. 9b). The chemical compositions of these precipitations

compose of Ca and O elements through the EDS analysis (Fig. 9c). These precipitations were identified as bone-like apatites, which are inspired by the apatite-forming capability of the Ti-25Nb alloy. Similar results can also be found in Ti/hydroxyapatite composites that the hydroxyapatite has a capability to stimulate the bone tissue formation [50]. The OH^- stretching vibration can be induced and acidic OH groups are bonded on Nb, resulting in the biocompatible surface of the alloy [1, 7]. Meanwhile, the hydroxyl groups accelerate the formation of calcium phosphates [51]. Therefore, the Ti-25Nb alloy can induce bone-like apatite nucleation and growth on their surfaces in the SBF solution, indicating its potential as a bioactive bone substitute.

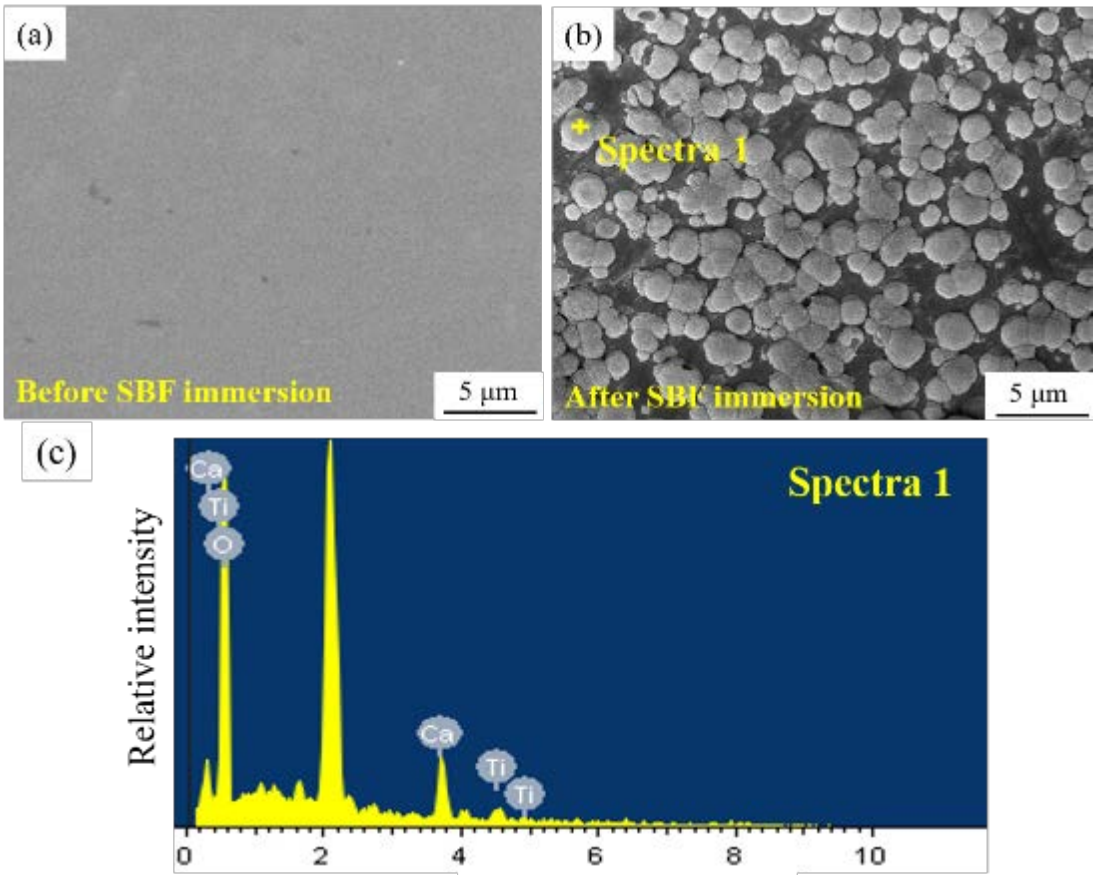

Fig. 9. *In vitro* bioactivity of the SLM-printed Ti-25Nb alloy at the energy density of E5: (a) and (b) surface morphologies before and after the SBF immersion, respectively, and (c) the EDS analyis of formed precipitations.

The initial reaction between cells and materials is of great essential for cell growth and differentiation. Fig. 10 shows the viability and spreading behavior of the cultivated osteoblasts on the surfaces of printed Ti-25Nb and pure Ti (blank group). According to

the immunofluorescence results, the green color represents filamentous actins and blue color fluorescence indicates the nuclides of the cells, as displayed in the confocal images (Figs. 10a and b). Compared to the pure Ti, the Ti-25Nb alloy was better colonized with cells covering most region, indicating the good cell-material interaction. Moreover, the osteoblasts adhered on the Ti-25Nb alloy exhibit a plumper with thick filopodia. The flourishing filopodia demonstrate that the cells experience a better growth and are more compatible with the Ti-25Nb alloy. The improved cell response can be related to the formation of Nb_2O_5 on the surface. Zhao *et al.* validated that the introduction of Nb_2O_5 enhanced the cell adhesion and proliferation by promoting the formation of extracellular matrix [52]. The OH^- combined with Nb also encouraged the cell adhesion by inducing the adsorption of cell adhesion-mediating proteins [53]. Therefore, the SLM-printed Ti-25Nb alloy not only possesses the superb *in vitro* biocompatibility but also has the potential to facilitate the growth of new bone tissue without a cytotoxic effect [54].

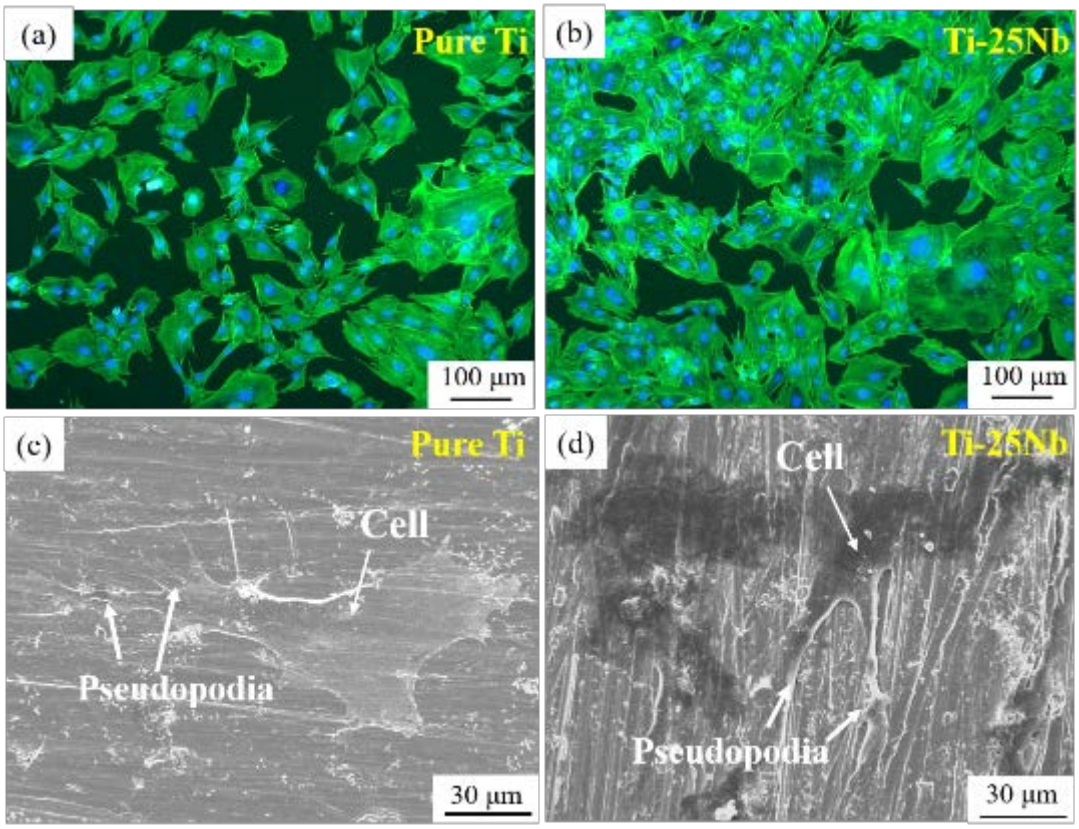

Fig. 10. Initial cell responses on the surfaces of the SLM-printed Ti-25Nb and pure Ti samples: (a) and (b) The immunofluorescence images, (c) and (d) SEM images.

4. Conclusions

The effect of laser energy density on the printability, phases, microstructure and mechanical properties of the Ti-25Nb alloy *in situ* fabricated by SLM using blended Ti and Nb elemental powders was systematically investigated in this work. The major findings are summarized as follows:

The energy density of 110 J/mm^3 results in the highest relative density of 97.5% and more homogeneous element distributions in the SLM-printed Ti-25Nb alloy. The α' martensite and β phases with an orientation relationship of [023]β // [-12-16]α' were identified. The proportion of α' phase tends to increase from 43% to 52%, and then decreases to 41% with the increase in energy density from 70 J/mm^3 to 110 J/mm^3. The augment of α' phase is ascribed to the high temperature gradient, and the reduction is due to the increase in β (Ti, Nb) solid solution from both the sufficient melting of Nb particles and diffusion of Ti and Nb elements.

With the increase in energy density, the microstructure of the printed Ti-25Nb alloy changes from α′ martensite acicular-shaped grains to coarsened lath-shaped grains and to lath-shaped + cellular-shaped subgrains, due to the decrease of cooling rate and the rise in temperature gradient.

The Ti-25Nb alloy printed using the energy density of 110 J/mm^3 achieves a superb combination of the high yield strength of 645 MPa, ultimate tensile strength of 748 MPa, ductility of 19.9%, and microhardness of 264 HV. The strengths and hardness of the alloy decrease with the increase of energy density from 70 J/mm^3 to 100 J/mm^3, and then increase to the highest at 110 J/mm^3. This variation is determined by both the coarsening of α' phase and the formation of β (Ti, Nb) solid solution. The SLM-printed Ti-25Nb alloy also exhibits both the superb apatite-forming capability and better cell spread and proliferation compared to pure Ti.

Acknowledgements

This work was supported by the National Natural Science Foundation of China (51775207), the National key R&D program of China, additive manufacturing and laser manufacturing key special subject of Chain (personalized implant prosthesis additive

manufacturing process research, 2016YFB1101303), the Academic frontier youth team at Huazhong University of Science and Technology, the Science and Technology Major Project of Guangdong Province (2017B090911007) and Application Fundamentals frontier Major Project of Wuhan (2018010401011281). The authors are also grateful for the State Key Laboratory of Materials Processing and Die & Mould Technology and the Analysis and Testing Center of Huazhong University of Science and Technology for all the measurements.

References

[1] Q. Wang, C. Han, T. Choma, Q. Wei, C. Yan, B. Song, Y. Shi, Materials & Design, 126 (2017) 268-277.

[2] J.P. Luo, J.F. Sun, Y.J. Huang, J.H. Zhang, Y.D. Zhang, D.P. Zhao, M. Yan, Materials Science and Engineering: C, (2018).

[3] L. Zhou, T. Yuan, R. Li, J. Tang, G. Wang, K. Guo, J. Yuan, Powder Technology, 342 (2019) 11-23.

[4] M. Niinomi, M. Nakai, J. Hieda, Acta Biomaterialia, 8 (2012) 3888-3903.

[5] Y. Li, Y. Ding, K. Munir, J. Lin, M. Brandt, A. Atrens, Y. Xiao, J.R. Kanwar, C. Wen, Acta Biomaterialia, (2019).

[6] D.R. Bloyer, R.O. Ritchie, K.T. Venkateswara Rao, Metallurgical and Materials Transactions A, 30 (1999) 633-642.

[7] I. Jirka, M. Vandrovcova, O. Frank, Z. Tolde, J. Plsek, T. Luxbacher, L. Bacakova, V. Stary, Mater Sci Eng C Mater Biol Appl, 33 (2013) 1636-1645.

[8] A. Bahador, E. Hamzah, K. Kondoh, T.A. Abu Bakar, F. Yusof, H. Imai, S.N. Saud, M.K. Ibrahim, Materials & Design, 118 (2017) 152-162.

[9] N.F. Daudt, F.J. Hackemüller, M. Bram, Materials Letters, 237 (2019) 161-164.

[10] M. Niinomi, Metallurgical and materials transactions A, 33 (2002) 477.

[11] J. Li, Z. Wei, L. Yang, B. Zhou, Y. Wu, S.-G. Chen, Z. Sun, Optik, (2019) 163760.

[12] M. Fischer, P. Laheurte, P. Acquier, D. Joguet, L. Peltier, T. Petithory, K. Anselme, P. Mille, Materials Science and Engineering: C, 75 (2017) 341-348.

[13] Y.J. Liu, H.L. Wang, S.J. Li, S.G. Wang, W.J. Wang, W.T. Hou, Y.L. Hao, R. Yang, L.C. Zhang, Acta Materialia, 126 (2017) 58-66.

[14] C. Han, C. Yan, S. Wen, T. Xu, S. Li, J. Liu, Q. Wei, Y. Shi, Rapid Prototyping Journal, 23 (2017) 16-27.

[15] C. Han, Y. Li, Q. Wang, S. Wen, Q. Wei, C. Yan, L. Hao, J. Liu, Y. Shi, J Mech Behav Biomed Mater, 80 (2018) 119-127.

[16] D. Zhao, Y. Huang, Y. Ao, C. Han, Q. Wang, Y. Li, J. Liu, Q. Wei, Z. Zhang, Journal of the Mechanical Behavior of Biomedical Materials, 88 (2018) 478-487.

[17] J.C. Wang, Y.J. Liu, P. Qin, S.X. Liang, T.B. Sercombe, L.C. Zhang, Materials Science and Engineering: A, 760 (2019) 214-224.

[18] J. Wei, H. Sun, D. Zhang, L. Gong, J. Lin, C. Wen, Materials, 12 (2018) 61.

[19] M. Fischer, D. Joguet, G. Robin, L. Peltier, P. Laheurte, Materials Science and Engineering: C, 62 (2016) 852-859.

[20] L. Thijs, F. Verhaeghe, T. Craeghs, J.V. Humbeeck, J.P. Kruth, Acta Materialia, 58 (2010) 3303-3312.

[21] G. Kasperovich, J. Haubrich, J. Gussone, G. Requena, Materials & Design, 105 (2016) 160-170.

[22] D.K. Do, P. Li, Virtual and Physical Prototyping, 11 (2016) 41-47.

[23] S.L. Sing, F.E. Wiria, W.Y. Yeong, International Journal of Refractory Metals and Hard Materials, 77 (2018) 120-127.

[24] L. Wanying, L. Yuanhua, C. Yuhai, S. Taihe, A. Singh, Rare Metal Materials and Engineering, 46 (2017) 634-639.

[25] T. Kokubo, H. Takadama, Biomaterials, 27 (2006) 2907-2915.

[26] D. Wang, C. Yu, J. Ma, W. Liu, Z. Shen, Materials & Design, 129 (2017) 44-52.

[27] R.I. Guthrie, T. Iida, The physical properties of liquid metals, Clarendon press, 1987.

[28] D. Gu, Y.-C. Hagedorn, W. Meiners, G. Meng, R.J.S. Batista, K. Wissenbach, R. Poprawe, Acta Materialia, 60 (2012) 3849-3860.

[29] C. Weingarten, D. Buchbinder, N. Pirch, W. Meiners, K. Wissenbach, R. Poprawe, Journal of Materials

Processing Technology, 221 (2015) 112-120.
[30] I. Polozov, V. Sufiiarov, A. Kantyukov, A. Popovich, Intermetallics, 112 (2019).
[31] R. Li, Y. Shi, J. Liu, Z. Xie, Z. Wang, The International Journal of Advanced Manufacturing Technology, 48 (2010) 597-605.
[32] B. AlMangour, D. Grzesiak, T. Borkar, J.-M. Yang, Materials & Design, 138 (2018) 119-128.
[33] B. Vrancken, L. Thijs, J.P. Kruth, J. Van Humbeeck, Acta Materialia, 68 (2014) 150-158.
[34] C.R. Hubbard, R.L. Snyder, Powder Diffraction, 3 (1988) 74-77.
[35] D. Moffat, U. Kattner, Metallurgical Transactions A, 19 (1988) 2389-2397.
[36] S.L. Sing, W.Y. Yeong, F.E. Wiria, Journal of Alloys and Compounds, 660 (2016) 461-470.
[37] M. Das, V.K. Balla, D. Basu, S. Bose, A. Bandyopadhyay, Scripta Materialia, 63 (2010) 438-441.
[38] D. Rosenthal, Transactions of ASME, 68 (1946) 849-866.
[39] W. Xu, M. Brandt, S. Sun, J. Elambasseril, Q. Liu, K. Latham, K. Xia, M. Qian, Acta Materialia, 85 (2015) 74-84.
[40] H. Nasiri-Abarbekoh, A. Ekrami, A.A. Ziaei-Moayyed, Materials & Design, 37 (2012) 223-227.
[41] X. Wu, C. Cai, L. Yang, W. Liu, W. Li, M. Li, J. Liu, K. Zhou, Y. Shi, Materials Science and Engineering: A, 738 (2018) 10-14.
[42] Y. Mantani, M. Tajima, Materials Science and Engineering: A, 438-440 (2006) 315-319.
[43] C.M. Lee, C.P. Ju, J.H. Chern Lin, 29 (2002) 314-322.
[44] H. Attar, S. Ehtemam-Haghighi, D. Kent, X. Wu, M.S. Dargusch, Materials Science and Engineering: A, 705 (2017) 385-393.
[45] T. Ahmed, H.J. Rack, Materials Science and Engineering: A, 243 (1998) 206-211.
[46] W. Yuan, S.K. Panigrahi, J.Q. Su, R.S. Mishra, Scripta Materialia, 65 (2011) 994-997.
[47] S.X. Liang, X.J. Feng, L.X. Yin, X.Y. Liu, M.Z. Ma, R.P. Liu, Materials Science and Engineering: C, 61 (2016) 338-343.
[48] Y. Bai, Y. Deng, Y. Zheng, Y. Li, R. Zhang, Y. Lv, Q. Zhao, S. Wei, Materials Science and Engineering: C, 59 (2016) 565-576.
[49] H. Attar, M. Calin, L.C. Zhang, S. Scudino, J. Eckert, Materials Science and Engineering: A, 593 (2014) 170-177.
[50] C. Ning, Y. Zhou, Biomaterials, 23 (2002) 2909-2915.
[51] Y.-J. Park, H.-J. Song, I. Kim, H.-S. Yang, Journal of Materials Science: Materials in Medicine, 18 (2007) 565-575.
[52] X. Zhao, G. Wang, H. Zheng, Z. Lu, X. Zhong, X. Cheng, H. Zreiqat, ACS Applied Materials & Interfaces, 5 (2013) 8203-8209.
[53] B. Feng, J. Weng, B. Yang, S. Qu, X. Zhang, Biomaterials, 24 (2003) 4663-4670.
[54] K. Miura, N. Yamada, S. Hanada, T.-K. Jung, E. Itoi, Acta Biomaterialia, 7 (2011) 2320-2326.